Separation Science and Technology
Publication details, including instructions for authors and subscription information:
http://www.informaworld.com/smpp/title~content=t713708471

Solvent Vapor Recovery by Pressure Swing Adsorption. III. Comparison of Simulation with Experiment for the Butane—Activated Carbon System

Yujun Liu[a]; Charles E. Holland[a]; James A. Ritter[a]
[a] DEPARTMENT OF CHEMICAL ENGINEERING, SWEARINGEN ENGINEERING CENTER, UNIVERSITY OF SOUTH CAROLINA, COLUMBIA, SOUTH CAROLINA, USA

Online publication date: 20 May 1999

SEPARATION SCIENCE AND TECHNOLOGY, **34**(8), pp. 1545–1576, 1999

Solvent Vapor Recovery by Pressure Swing Adsorption. III. Comparison of Simulation with Experiment for the Butane–Activated Carbon System

YUJUN LIU, CHARLES E. HOLLAND, and JAMES A. RITTER*
DEPARTMENT OF CHEMICAL ENGINEERING
SWEARINGEN ENGINEERING CENTER
UNIVERSITY OF SOUTH CAROLINA
COLUMBIA, SOUTH CAROLINA 29208, USA

ABSTRACT

A fully predictive (no adjustable parameters), nonisothermal, multicomponent mathematical model was developed and used to simulate a pressure swing adsorption (PSA) process designed for the separation and recovery of concentrated butane vapor from nitrogen using BAX activated carbon. Nearly quantitative agreement with experiment was realized with this model over a wide range of process conditions, and for both the transient and periodic state process dynamics and the periodic state process performance. The model also verified some unique characteristics of this PSA process, and it revealed some of the subtleties associated with accurately simulating a PSA–solvent vapor recovery (SVR) process. These subtleties included the need to account for the adsorbate heat capacity and the temperature dependence of the gas-phase physical properties. No PSA models in the literature have included both of these features, which were critical to the accurate prediction of the heat effects in this PSA–SVR process.

INTRODUCTION

Experimental investigations are absolutely necessary in the design and development of pressure swing adsorption (PSA) processes, especially new PSA processes like PSA–solvent vapor recovery (SVR). However, experi-

* To whom correspondence should be addressed. Telephone: (803) 777-3590. FAX: (803) 777-8265. E-mail: ritter@sun.che.sc.edu

ments can be time-consuming and cost-ineffective. For instance, a PSA–butane–activated carbon process with a 20-minute cycle time may take about 200 cycles to reach the periodic state, depending on the process conditions (1, 2). As a cost-effective alternative to experimentation, mathematical models have been widely used in the study of PSA processes (3, 4); however, the validation of such models with rigorous experimentation is sometimes lacking, yet crucial.

The mathematical models of a PSA process can be classified into two categories: equilibrium theory models and rigorous numerical models. An equilibrium theory model was first developed by Shendalman and Mitchell (5) for a single adsorbable species; this model was extended to a system with two adsorbable components by Chan et al. (6) and to bulk separation of a binary mixture by Flores and Kenney (7) and Knaebel and Hill (8). More recently, equilibrium theory has been developed for PSA–SVR (9–11), where, under certain simplifying assumptions, analytical expressions were obtained to predict directly the periodic state PSA–SVR process performance and bed profiles (9, 10). These analytic PSA models can be used to provide preliminary design guidance and useful insight into the system behavior at the periodic state (10). However, equilibrium theory does not afford an easy extension to more realistic situations, and it does not allow the approach to the periodic state to be simulated very easily. Yet the transient process dynamics can be very different from those at the periodic state, especially the transient thermal behavior in PSA–SVR (1, 2); and the analysis and design can be very complex with the effects of some of the parameters being coupled (12).

An evaluation of the most prevalent approximations used in PSA–SVR mathematical models showed that the assumptions utilized in the equilibrium theory models can lead to rather large deviations from the rigorous model (13). Unlike the equilibrium theory approach, dynamic simulation involves tracking the transient by repeated numerical integration of the governing equations until the periodic state is reached. This numerical approach thus provides greater flexibility and greater accuracy in aiding process designers in the quest for achieving a satisfactory, cost-effective, and practical design. But of course the penalty to be paid is the expense of increased computation time compared to the equilibrium theory approach.

In Parts I and II of this series the experimental transient and periodic dynamics and the periodic performance of the recovery of butane vapor from nitrogen using BAX activated carbon in a unique PSA system were reported (1, 2). These experimental studies revealed several interesting features of PSA–SVR systems. For example, no multiplicity exists when a PSA–SVR process starts from columns that are less contaminated initially than at the periodic state; high transient temperatures may occur inside the column even when the PSA–SVR process starts from partially contaminated columns; and

high solvent vapor concentrations approaching saturation may be obtained during the blowdown step under certain circumstances. Clearly, this kind of comprehensive experimental data can be used as a stringent test for validation of a rigorous PSA model. Therefore, the objective of Part III is to demonstrate the use of a fully predictive (no adjustable parameters), rigorous mathematical model for simulating the PSA–butane vapor recovery process. By comparing the simulation results with the experimental results reported in Parts I and II (1, 2), the strengths and weaknesses of this model are revealed along with the needs for accurately predicting the PSA–SVR process dynamics and performance.

MATHEMATICAL MODEL

The development of mathematical models that describe the PSA process have gradually evolved by sequentially eliminating certain simplifying assumptions (4, 13). Because of the complexity and nature of PSA processes, some common assumptions have been utilized frequently in PSA models. These include: ideal gas law, negligible column pressure drop, thermal equilibrium between gas and solid phases, plug flow, negligible axial and radial dispersions, negligible axial heat conduction, and temperature-independent adsorbent properties. These simplifying assumptions are also used to establish the multicomponent mathematical model of this PSA–SVR process. In addition, this PSA model accounts for integration of the pressurization and blowdown steps, gas-phase velocity variations during each step, and finite mass and heat transfer resistances.

The mass transfer mechanism from the bulk gas phase into the adsorbent can be described either by the rigorous pore diffusion model (14–18) or the linear driving force (LDF) approximation (19–23). Although the pore diffusion model is more realistic, the associated computational time is lengthy, and it offers little advantage over the LDF model for equilibrium-controlled PSA (4). Thus, the LDF approach is used in this work.

The amplitude of the temperature swing in PSA–SVR depends primarily on the heat of adsorption, the throughput, and the heat transfer characteristics of the packed adsorbent column (22). The choice of an appropriate model to account for heat transfer in the energy balance is also critical to any realistic, dynamic PSA simulation. A detailed heat balance should include equations describing the gas phase, adsorbed phase, and the column wall heat balance. In this model, however, the heat transfer is accounted for by an overall heat transfer coefficient to save computational time and because it has been shown that the major resistance to heat transfer in fixed-bed adsorption processes is at the wall of cylindrical columns (24). Different from most PSA models in the literature, this PSA model also accounts for the temperature dependence of the

gas-phase physical properties, the heat capacity of the adsorbed phase, and the loading dependence of the heat of adsorption.

For a feed mixture consisting of N components, the total mass balance is given by

$$\frac{\partial u}{\partial z} - \frac{1}{T}\frac{\partial T}{\partial t} + \frac{1}{P}\frac{\partial P}{\partial t} - \frac{u}{T}\frac{\partial T}{\partial z} + \sum_{i=1}^{N} S_i = 0 \tag{1}$$

where

$$S_i = \frac{1-\varepsilon}{\varepsilon}\frac{RT\rho_s}{P}\frac{\partial q_i}{\partial t}, \qquad i = 1, 2, \ldots, N \tag{2}$$

and $\partial q_i/\partial t$ is based on the LDF approximation as

$$\frac{\partial q_i}{\partial t} = k_i(q_i^* - q_i), \qquad i = 1, 2, \ldots, N \tag{3}$$

The component mass balances are given by

$$\frac{\partial y_i}{\partial t} + u\frac{\partial y_i}{\partial z} - y_i\sum_{j=1}^{N} S_j + S_i = 0, \qquad i = 1, 2, \ldots, N-1 \tag{4}$$

and the energy balance is written as

$$\frac{\partial(uCp_g)}{\partial z} + \left(\frac{Cp_g}{P}\frac{\partial P}{\partial t} + \frac{\partial Cp_g}{\partial t}\right) + \rho_s Cp_s\frac{1-\varepsilon}{\varepsilon}\frac{R}{P}\frac{\partial T}{\partial t} + \frac{1-\varepsilon}{\varepsilon}\frac{R}{P}\rho_s\frac{\partial\left[\sum_{i=1}^{N} q_i(Cp_{ai}T + \Delta H_i)\right]}{\partial t} + \frac{2h}{\varepsilon r_b}\frac{R}{P}(T - T_0) = 0 \tag{5}$$

The gas-phase heat capacity is given by

$$Cp_g = \sum_{i=1}^{N} y_i\, Cp_{gi} \tag{6}$$

where

$$Cp_{gi} = A_i + B_iT + C_iT^2 + D_iT^3, \qquad i = 1, 2, \ldots, N \tag{7}$$

The single and mixed-gas equilibrium amounts adsorbed are represented by the three process Langmuir model (TPLM) (23, 25), which is modified here for mixtures as

$$q_i^* = \sum_{j=1}^{3} \frac{q_{i,j}^s b_{i,j} P y_i}{1 + \sum_{i=1}^{N} b_{i,j} P y_i} \qquad i = 1, 2, \ldots, N \tag{8}$$

where

$$b_{i,j} = b_{i,j}^0 \exp\left(\frac{B_{i,j}}{T}\right) \tag{9}$$

The initial and boundary conditions depend on the PSA–SVR process configuration being utilized. In Parts I and II of this series, all of the PSA–SVR processes were started from Step II. For a process that starts from clean beds, the initial conditions of the process, i.e., the initial conditions of the first cycle, are

Step II: at $t = 0$: $y_i = 0$, $T = T_0$, $q_i = 0$, for all z

For a process that starts from the periodic state of a previous run, the initial conditions of the first cycle are

Step II: at $t = 0$: $y_i = y_{i,\,\mathrm{I,\,pps}}$ $T = T_{\mathrm{I,\,pps}}$, $q_i = q_{i,\,\mathrm{I,\,pps}}$, for all z

where the subscript pps represents the "previous periodic state." For subsequent cycles, the initial and boundary conditions for each step are given below and they apply to all cycles whether the process starts from clean or contaminated beds.

Step I:	at $t = 0$:	$y_i = y_{i,\,\mathrm{IV}}$,	$T = T_{\mathrm{IV}}$,	$q_i = q_{i,\,\mathrm{IV}}$,	for all z
	at $z = 0$:	$u = 0$			for all t
	at $z = L$:	$y_{\mathrm{butane}} = 0$	$y_{\mathrm{nitrogen}} = 1$	$T = T_0$	for all t
Step II:	at $t = 0$:	$y_i = y_{i,\,\mathrm{I}}$,	$T = T_{\mathrm{I}}$,	$q_i = q_{i,\,\mathrm{I}}$,	for all z
	at $z = 0$:	$y_i = y_{i,\,\mathrm{f}}$,	$T = T_{\mathrm{f}}$,	$u = u_{\mathrm{f}}$	for all t
Step III:	at $t = 0$:	$y_i = y_{i,\,\mathrm{II}}$,	$T = T_{\mathrm{II}}$,	$q_i = q_{i,\,\mathrm{II}}$,	for all z
	at $z = L$:	$u = 0$			for all t
Step IV:	at $t = 0$:	$y_i = y_{i,\,\mathrm{III}}$,	$T = T_{\mathrm{III}}$,	$q_i = q_{i,\,\mathrm{III}}$,	for all z
	at $z = L$:	$y_i = y_{i,\,\mathrm{II}}(t)$,	$T = T_{\mathrm{II}}(t)$,	$u = u_{\mathrm{P}}$	for all t

Equations (1) to (9), along with the set of initial and boundary conditions, represent the comprehensive mathematical model of a multicomponent PSA–SVR process. This model was solved using a finite difference scheme. Details of the solution method are given elsewhere (22, 26).

EXPERIMENTAL

The apparatus and procedure for the PSA–butane–nitrogen–BAX activated carbon experimental system were described in detail in Part I (1). The basic information regarding this apparatus that was needed for the simulation is listed in Table 1. A four-step Skarstrom-type PSA cycle was utilized with the four steps consisting of (I) countercurrent pressurization by pure nitrogen, (II) cocurrent high pressure adsorption, (III) countercurrent blowdown, and (IV) countercurrent light product purge. In Parts I and II, six series of experimental runs were carried out to investigate the transient and periodic process dynamics, and the effects of six process parameters on the process performance, i.e., the effects of the purge-to-feed ratio (γ), purge pressure (P_L), volumetric flow rate (V_f), feed mole fraction (y_f), cycle time (t_c), and pressurization/blowdown step time (t_{pb}). In each series of runs the process was always started using the value of the parameter of interest that resulted in the smallest periodic state concentration wave penetration, and after all of the necessary information was collected at the periodic state, the value of this parameter was shifted to the next value which gave the second smallest bed penetration without stopping the experiment and regenerating the columns. The experiment was stopped and the columns were regenerated only when a series of runs designed to study the process parameter of interest were completed. It was experimentally verified that operating in this sequential manner leads to valid results because a unique periodic state was obtained for a set of process conditions whether the process was started from a completely regenerated or initially contaminated bed, as long as the periodic state resulted in a more contaminated bed compared to the initial condition (1).

The PSA–SVR periodic state process performance was analyzed according to the solvent vapor enrichment (E) and recovery (R), the light product purity

TABLE 1
Bed Characteristics of the Twin Bed PSA-SVR Apparatus[a] and the Transport Properties

Bed radius	0.0387 m
Bed length	0.2724 m
Packing void fraction	0.391
Pellet density	550.0 kg/m^3
Pellet radius	0.00105 m
Adsorbent bed loading	430.0 g
Mass transfer coefficient	0.027 s^{-1}
Overall heat transfer coefficient	0.00067 kJ/m^2·s·K

[a] The apparatus is described in detail elsewhere (1).

(y_p), and the bed capacity factor (BCF). These indicators were defined and the calculational procedure from experimental data were described in Part II (2). The same definition and calculational procedures are employed in this mathematical modeling study for all of the indicators except for the BCF. From simulation results, the BCF was obtained strictly from the definition (22), which is

$$\text{BCF} = \int_0^L q\, dz / q_f^* L \tag{10}$$

From experimental results, however, the BCF was approximated using a modified form of Eq. (10) since the adsorbed phase loadings were not measured directly, i.e., q in Eq. (10) was replaced by q^*, the equilibrium amount of butane adsorbed corresponding to the gas-phase concentration that was measured experimentally (2).

MODEL PARAMETER DETERMINATION

Adsorption Isotherms

The three process Langmuir model isotherm parameters were obtained from regressed experimental data for nitrogen and butane adsorbed on BAX activated carbon (27). The parameters are given in Table 2, along with the absolute relative error (ARE) of the correlations, which is defined as

$$\text{ARE} = \frac{100}{N} \sum_{i=1}^{N} \text{abs}\left(\frac{q_{\text{exp},i} - q_{\text{cal},i}}{q_{\text{exp},i}}\right)\% \tag{11}$$

The ARE's for both adsorbates were very low, indicating a good fit of the model to the experimental data.

Heats of Adsorption

The heat of adsorption of each component was assumed to be the same as that of the corresponding single component, and the loading dependency of the heat of adsorption was calculated from the adsorption isotherms (28) and then regressed into a polynomial of the form

$$\Delta H_i = c_0 + c_1 q + c_2 q^2 + c_3 q^4 + c_4 q^5 \tag{12}$$

The polynomial coefficients are also given in Table 2.

TABLE 2
Values of the Parameters Used in the PSA Model

	Parameters for the gas-phase heat capacity, Cp_g [kJ/(mol·K)]			
	$A \times 10^2$	$B \times 10^4$	$C \times 10^7$	$D \times 10^{11}$
n-Butane	0.948	3.310	−1.107	−0.282
Nitrogen	3.112	−0.136	0.268	1.167

	Parameters for the three process Langmuir model			
		q_m	b_0	B
n-Butane–BAX (ARE: 3.0%)	Process 1	6.4627	1.5091×10^{-8}	3968.5822
	Process 2	2.6820	7.2187×10^{-8}	4653.4317
	Process 3	0.7305	5.3529×10^{-8}	6009.3764
Nitrogen–BAX (ARE: 3.96%)	Process 1	1.2163	6.8751×10^{-5}	720.8872
	Process 2	2.1379	4.2256×10^{-8}	2552.3570
	Process 3	0.0189	2.0223×10^{-33}	21347.0611

	Coefficients for the isosteric heat of adsorption, ΔH (kJ/mol)				
	c_0	c_1	c_2	c_3	c_4
n-Butane	−53.879	14.466	−4.753	0.744	−0.041
Nitrogen	−44.105	55.222	366.376	−1706.729	1831.544

Adsorbed-Phase Heat Capacities

The adsorbed-phase heat capacities of butane and nitrogen were approximated by the corresponding gas-phase heat capacities, based on results obtained from thermodynamic correlations derived from the adsorption isotherms for several hydrocarbons adsorbed on BAX carbon (27). Their values were taken at room temperature as 0.0986 kJ/mol·K for butane and 0.0284 kJ/mol·K for nitrogen.

Pressure History

The pressure history is required as input to the PSA model. The pressure was held constant at P_H and P_L during the adsorption and purge steps, respectively. To better represent the real situation, some researchers have used the experimentally measured pressure histories during the pressurization and blowdown steps in their mathematical models (16–18). To keep the model fully predictive, however, the pressure histories were approximated here by linear functions of time during the blowdown and pressurization steps.

Mass Transfer Coefficients

The butane mass transfer coefficient in the LDF approximation (Eq. 3) was calculated according to $k = 15D_e/r_p^2$, where D_e was measured experimentally by the uptake method proposed by Ruthven (29). The uptake experiments were carried out gravimetrically at different *n*-butane mole fractions ranging from 5 to 100%. An average D_e was used to calculate k using a pellet radius of 1.05 mm. The same mass transfer coefficient was used for nitrogen. The value is given in Table 1.

Heat Transfer Coefficient

The overall heat transfer coefficient (h) in the energy balance (Eq. 5) was determined experimentally. One of the two PSA columns was used to carry out adsorption breakthrough experiments of nitrogen. The column was filled initially with helium at the operating pressure, and then after initiating the flow of nitrogen (2.0 SLPM), the temperature histories at different positions inside the bed were recorded as a function of time by the nine in-bed thermocouples (1). These recorded temperature breakthroughs were then used to calculate the overall heat transfer coefficient by using the thermal wave method proposed by Kaguei et al. (30). Pure nitrogen was used because it produced smaller temperature changes inside the column which made the assumptions utilized in the development of the thermal wave method more accurate (such as the temperature-independent physical property assumption). The overall heat transfer coefficient determined by this method is given in Table 1. It is noted that the heat transfer coefficient is generally a function of the volumetric flow rate; however, in this PSA model a constant h was used for simplicity.

RESULTS AND DISCUSSION

Each of the six series of experiments (1, 2) were simulated using the rigorous mathematical model described above. The values of the process parameters, i.e., the purge-to-feed ratio (γ), purge pressure (P_L), volumetric flow rate (V_f), feed concentration (y_f), cycle time (t_c), and pressurization/blowdown step time (t_{pb}) were taken directly from the experimental results reported in Part I (1); they are reproduced in Table 3, along with the periodic state process performance determined from both the experiments and simulations. Since detailed explanations of the experimental results have been given in Parts I and II of this series (1, 2), they are not repeated here. In contrast, the discussion below focuses on the comparison of the simulation results with the experimental results to examine how well the strictly predictive PSA model performs and to expose subtleties associated with modeling PSA–SVR processes.

TABLE 3
PSA-SVR Process Conditions[a] and Process Performance[b]

Run	V_f (SLPM)	γ (—)	y_f (%)	t_c (min)	t_{pb} (min)	P_L (kPa)	E (—)	R (%)	BCF (—)	y_p (—)
A1	2.5	*1.41*	*21.2*	20	2	*14.7*	1.98 (2.26)	100 (100)	0.31 (0.29)	0.0 (0.0)
A2	2.5	*1.28*	20.8	20	2	13.5	2.11 (2.55)	100 (100)	0.32 (0.33)	0.0 (0.0)
A3	2.5	*1.14*	21.8	20	2	12.2	2.27 (2.72)	100 (100)	0.34 (0.36)	0.0 (0.0)
A4	2.5	*0.50*	20.4	20	2	13.7	2.75 (3.62)	100 (100)	0.49 (0.44)	0.0 (0.0)
A5	2.5	*0.24*	20.8	20	2	14.6	3.14 (4.22)	92.7 (85.9)	0.76 (0.81)	0.017 (0.034)
B1	2.5	1.45	19.9	20	2	*28.3*	1.64 (1.80)	100 (100)	0.34 (0.30)	0.0 (0.0)
B2	2.5	1.49	20.3	20	2	*41.4*	1.38 (1.55)	100 (100)	0.35 (0.31)	0.0 (0.0)
B3	2.5	1.48	19.6	20	2	*55.7*	1.22 (1.46)	100 (100)	0.36 (0.35)	0.0 (0.0)
B4	2.5	1.50	20.4	20	2	*68.8*	1.08 (1.40)	100 (100)	0.36 (0.38)	0.0 (0.0)
C1	*1.5*	1.48	19.7	20	2	13.9	1.87 (2.01)	100 (100)	0.17 (0.17)	0.0 (0.0)
C2	*2.5*	1.50	20.9	20	2	13.8	1.97 (2.32)	100 (100)	0.29 (0.30)	0.0 (0.0)
C3	*3.5*	0.86	20.6	20	2	23.9	2.31 (2.95)	99.2 (97.2)	0.71 (0.74)	0.0046 (0.0067)
C4	*4.0*	0.80	20.6	20	2	26.5	2.35 (3.12)	96.9 (91.9)	0.81 (0.83)	0.015 (0.019)
D1	2.5	1.41	*9.5*	20	2	14.6	2.78 (3.30)	100 (100)	0.22 (0.22)	0.0 (0.0)
D2	2.5	1.17	*31.4*	20	2	17.6	1.60 (1.67)	100 (100)	0.40 (0.38)	0.0 (0.0)
D3	2.5	0.94	*39.3*	20	2	22.0	1.45 (1.54)	100 (100)	0.48 (0.62)	0.0 (0.0)
E1	2.5	0.74	34.0	*10*	1.0	27.7	1.41 (1.42)	100 (100)	0.30 (0.32)	0.0 (0.0)
E2	2.5	0.73	34.9	*15*	1.5	28.3	1.52 (1.71)	100 (100)	0.47 (0.47)	0.0 (0.0)
E3	2.5	0.69	35.8	*20*	*2.0*	29.8	1.63 (2.01)	99.3 (99.0)	0.65 (0.73)	0.00034 (0.0058)
E4	2.5	0.73	35.3	*25*	2.5	28.4	1.66 (1.96)	98.2 (97.8)	0.74 (0.81)	0.007 (0.013)
E5	2.5	0.76	35.6	*30*	3.0	26.9	1.69 (1.95)	96.4 (92.4)	0.80 (0.82)	0.03 (0.044)
F1	2.5	0.76	34.5	26	*5*	27.2	1.65 (2.04)	99.2 (99.4)	0.64 (0.67)	0.0042 (0.0036)
F2	2.5	0.75	34.9	24	*4*	27.3	1.65 (2.06)	99.2 (99.3)	0.64 (0.71)	0.0045 (0.0042)
F3	2.5	0.74	34.4	22	*3*	27.8	1.67 (2.00)	99.2 (99.0)	0.64 (0.73)	0.0034 (0.0058)

[a] The adsorption (Step II) pressure for all runs was approximately 151.6 kPa.
[b] Experimental results are in parentheses; values in italics denote the varied parameter.

Prediction of the Transient and Periodic State Process Dynamics

The experiments in Parts I and II (as explained above) were carried out by starting a series of runs from the value of the parameter of interest that gave the smallest bed penetration; thus, it is important to know whether a PSA process based on a specific set of conditions reaches the same or different periodic state as that when the process starts from clean beds. The experimental results showed that a unique periodic state is reached for a PSA process operated in this way. A stringent test of the PSA model was to examine whether it also predicted this behavior.

Simulation and experimental results of the butane vapor concentration and temperature profiles at the beginning and end of the adsorption step of Run E3 are plotted in Fig. 1 for processes that were started from clean beds and from the periodic state condition of Run E2. The model predicted only one periodic state in agreement with the experiments, whether the process was started from clean beds or from the periodic state of Run E2. Moreover, the model predicted the bed profiles quite satisfactorily, except for the temperatures in the mass transfer zone at the beginning of the adsorption step, where the predicted temperatures were relatively high compared to the experimentally measured temperatures. As reported in the literature, the temperature profile at the beginning of the adsorption step (i.e., at the end of the pressurization step) does not change much from the temperature profile at the end of the purge step (1, 22). Thus, the overprediction of the mass transfer zone temperatures essentially stemmed from the overprediction of the temperatures during the desorption steps. Several reasons may have contributed to the overprediction of the desorption temperatures; the most important one was perhaps the constant overall heat transfer coefficient utilized in the PSA model. During the desorption steps, especially the blowdown step, the gas-phase velocity inside the column changed dramatically with time, with the highest velocity being several decades higher than the feed velocity; this necessarily increased the heat transfer coefficient. An increased heat transfer coefficient would enhance the heat transfer from the high temperature columns to the ambient, resulting in lower blowdown and hence purge step temperatures.

Figure 2 compares the simulated and experimental transient butane vapor concentration (Fig. 2a) and temperature histories at the end of the adsorption step for different positions in the column for Run E3 that was started from clean beds. In Fig. 2(a), only the simulated butane vapor mole fractions are displayed since the transient gas-phase concentration samples were not taken during the experimental run. In Fig. 2(b), only the temperatures at four of the nine thermocouple positions are displayed so as not to crowd the figure. Figure 2(a), clearly shows the gradual progress of the concentration wave front

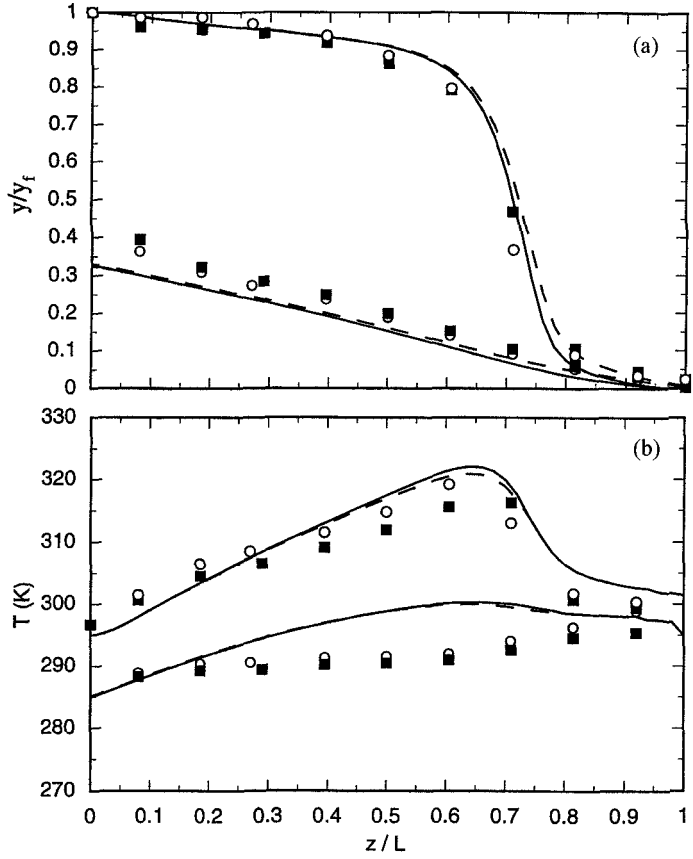

FIG. 1 Periodic state (a) gas-phase mole fraction and (b) temperature profiles at the beginning and end of the adsorption step of Run E3. Symbols: experiment; lines: simulation; solid lines and filled symbols represent results of the run started from clean beds; dashed lines and empty symbols represent results started from the periodic state of Run E2.

along the axial direction of the column during the transient approach to the periodic state. For example, the butane vapor reached $z/L = 0.71$ (Position 7) at the end of the adsorption step of Cycle 5, whereas $z/L = 0.91$ (Position 9) was barely contaminated by the butane vapor after 100 cycles. The mathematical model also predicted the transient temperatures very well, as shown in Fig. 2(b). The simulation successfully captured the high transient temperatures as well as the movement of the temperature wave through the column from Positions 1 to 9.

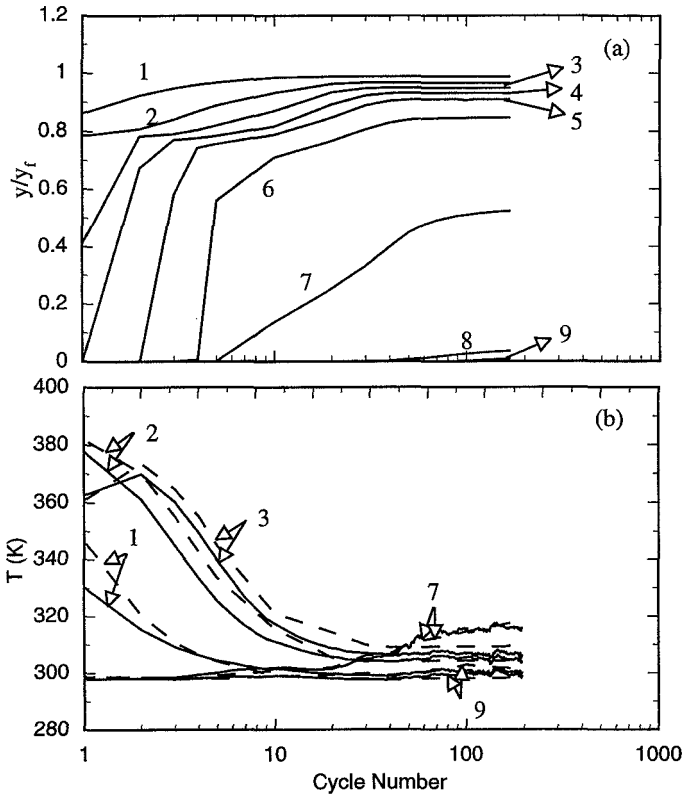

FIG. 2 Transient (a) butane vapor mole fraction (modeling results only) and (b) temperature histories as a function of the cycle number at the end of the adsorption step at different positions in the bed for Run E3 that was started from clean beds. Dashed lines: simulation; solid lines: experiment. Numbers 1 to 9 represent the position of z/L = 0.08, 0.185, 0.29, 0.395, 0.5, 0.605, 0.71, 0.815, and 0.92, respectively.

It is also interesting to note that the number of cycles taken by the PSA model to reach the periodic state (168 cycles) was also very close to that observed experimentally (about 160 cycles). This agreement was also true for the simulation of other runs. As examples, it took about 146 cycles for Run E1 to reach the periodic state experimentally, whereas the model predicted 141 cycles; and it took about 120 cycles for Run F1 to reach the periodic state experimentally, whereas the model predicted 131 cycles.

Figure 3 shows the differences in the pressure and ambient temperature histories for this run. Figure 3(a) shows that the linear pressure history dur-

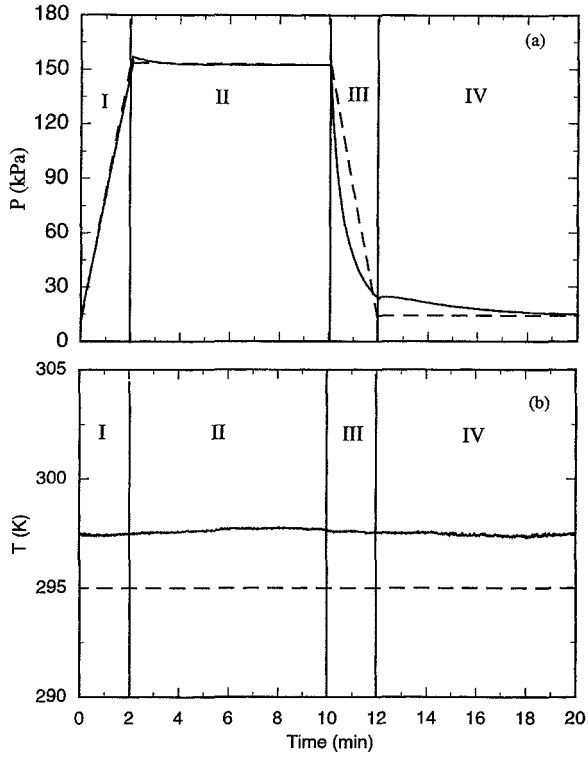

FIG. 3 (a) Pressure and (b) ambient temperature histories during a complete periodic state cycle for Run A1. Solid lines: experiment; dashed lines: simulation.

ing the pressurization step and a constant pressure during the adsorption step were very good assumptions. However, the linear pressure history during the blowdown step deviated from the experimentally measured pressure history, and so did the constant pressure assumption during the purge step, especially at the initial stages of blowdown. During most of the blowdown step, the experimental depressurization rate was much higher than the linearly decreasing rate as shown in Fig. 3(a). It is noted, however, that no attempt was made to control the depressurization rate during an experimental run, except to reach the purge pressure (P_L) by the end of Step IV (1). So the depressurization rate was essentially determined by the flow characteristics of the experimental system.

The experimental ambient temperatures varied from run to run because of the length of time it took to complete a run. However, a constant ambient tem-

perature (T_0 = 295 K) was used throughout all of the simulations in an effort to make the model fully predictive. Nevertheless, the difference between the ambient temperature histories for Run A1 shown in Fig. 3(b) was typical of all of the runs; so the use of 295 K was a reasonable choice.

The predicted butane vapor concentration and temperature histories during the periodic state at different positions are displayed in Fig. 4 for Run A1. In Fig. 4(b), the experimentally measured temperature histories are compared with those from simulations at four representative positions. Figure 4(a)

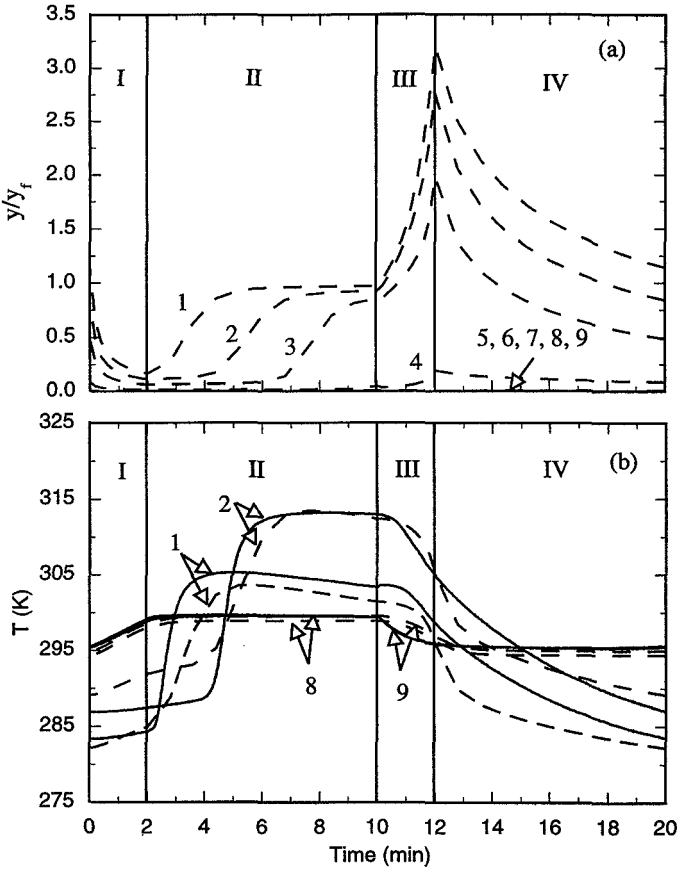

FIG. 4 (a) Butane vapor mole fraction histories (simulated only) and (b) temperature histories at different positions in the column during a complete periodic state cycle for Run A1. Dashed lines: simulation; solid lines: experiment. Numbers 1 to 9 represent the positions of z/L = 0.08, 0.185, 0.29, 0.395, 0.5, 0.605, 0.71, 0.815, and 0.92, respectively.

clearly shows the movement of the butane vapor concentration wave. During the periodic state, Position 4 ($z/L = 0.395$) was only slightly contaminated, whereas Positions 5 to 9 were completely free of butane. Figure 4(a) also shows how the butane vapor became enriched during the blowdown and purge steps, the trends of which were quite similar to the effluent histories shown in Part I (1). The model also satisfactorily predicted the temperature histories as shown in Fig. 4b. The coincidence between the time when the concentration wave (Fig. 3a) and the temperature wave (Fig. 4b) reached a certain position verified the statement made in Part I of this series that the position of the temperature wave front was indicative of the position of the concentration wave front. The model also successfully predicted the temperature swings during the periodic state cycle that were caused by adsorption and desorption of the carrier gas (nitrogen) as illustrated in Fig. 4(b) (Positions 8 and 9). The differences between the predicted and experimental temperature histories at these solvent vapor-free positions (Positions 8 and 9) during the blowdown step and in the mass transfer zone regions (Positions 1 and 2) during the initial stages of the purge step may have been caused by the differences in the pressure histories during these two steps (Fig. 3a). Deviations between the modeling and experimental results may have also been caused by the use of the mixed-gas TPLM, which has not been validated against any binary experimental data. Nevertheless, the agreement between the modeling and experimental temperature histories gave some confidence in the model parameters, especially the independently measured heats of adsorption, adsorbed phase heat capacities, and overall heat transfer coefficient.

Prediction of the Periodic State Process Performance

The predicted process performance from the PSA model, i.e., the butane vapor recovery (R) and enrichment (E), the light product purity (y_p), and the bed capacity factor (BCF) are tabulated in Table 3 for each run along with the experimental results. The simulated and experimental periodic state butane vapor concentration and temperature profiles, and the process performance indicators are compared in Figs. 5 to 16 for the six parameters investigated. Each of these parameters is discussed in turn below.

The simulated butane vapor concentration and temperature profiles at the beginning and end of the adsorption step of the series of runs (Runs A1 to A5) that were carried out to investigate the effect of the purge-to-feed ratio (γ) are compared with the experimental profiles in Fig. 5. A comparison of the simulated and experimental process performances from these runs is given in Fig. 6. Only the profiles for three of the fives runs are plotted for clarity. The model was fully capable of predicting these profiles. Interestingly, the predicted peak temperature for Run A1 was located at a position between $z/L = 0.29$ and

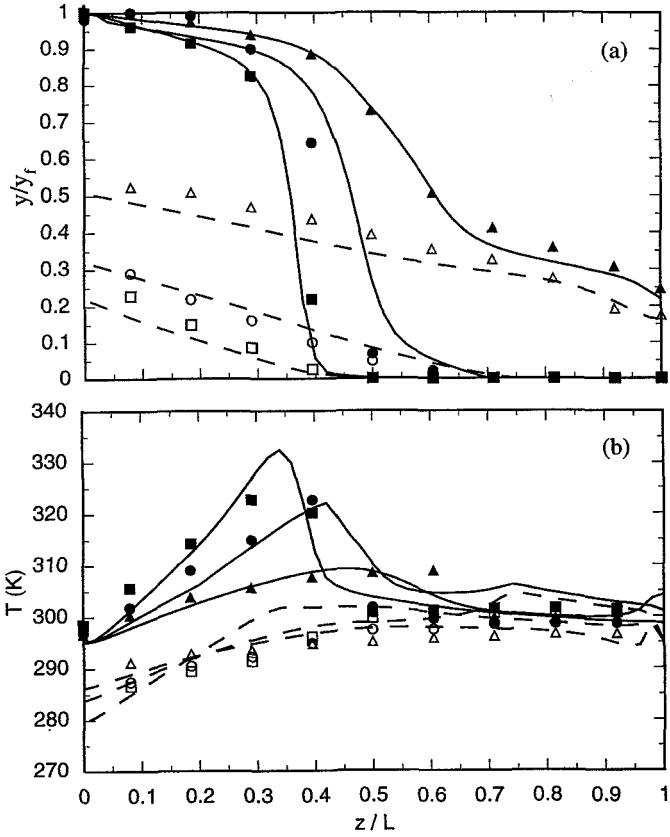

FIG. 5 Effect of the purge-to-feed ratio (γ) on the (a) gas-phase mole fraction and (b) temperature profiles at the beginning (dashes) and end (solid lines) of the adsorption step. Symbols: experiment; lines: simulation; (■, □) Run A1; (●, ○) Run A4; (▲, △) Run A5.

0.395; and it was about 10 K higher than the peak temperature reported experimentally (2), which was limited by the number and position of the thermocouples in each column. While the prediction of the BCF for all of the runs was almost quantitative, the predicted E's were consistently lower than those from the experiments, with the percentage differences ranging from -12.3% for Run A1 to -25.5% for Run A5. The y_p and R predictions were quantitative for runs without breakthrough; but for Run A5, which had significant breakthrough, the model predicted a lower y_p and a higher R. Nevertheless, the

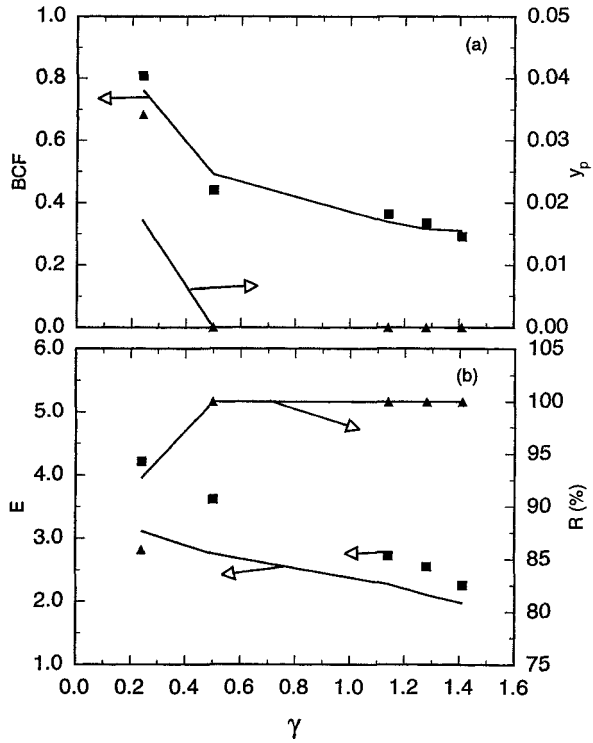

FIG. 6 Effect of the purge-to-feed ratio (γ) on the process performance in terms of the bed capacity factor (BCF), light product purity (y_p), butane vapor enhancement (E), and solvent vapor recovery (R). Symbols: experiment; lines: simulation.

results were quite satisfactory when considering that no adjustable parameters were used in this PSA model.

The simulated butane vapor concentration and temperature profiles at the beginning and end of the adsorption step of the series of runs (Runs A1, and B1 to B4) that were carried out to investigate the effect of the purge pressure (P_I) are compared with the experimental profiles in Fig. 7. A comparison of the simulated and experimental process performances from these runs is given in Fig. 8. It was interesting that the model also predicted that P_L had essentially no effect on the bed profiles, in agreement with the experimental results (Fig. 7). Since no breakthrough occurred in this series of runs, the process per-

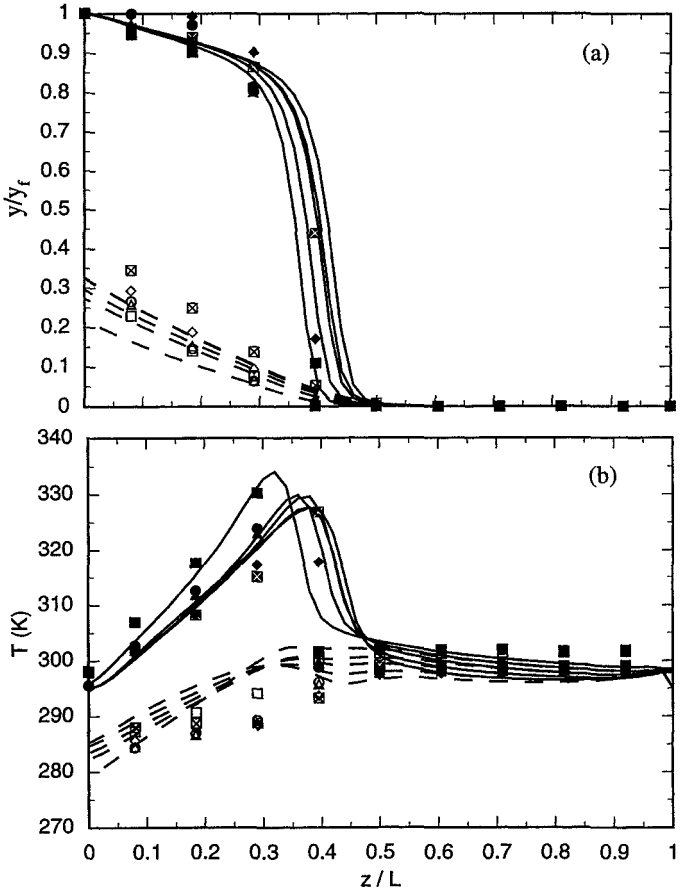

FIG. 7 Effect of the purge pressure (P_L) on the (a) gas-phase mole fraction and (b) temperature profiles at the beginning (dashes) and end (solid lines) of the adsorption steps. Symbols: experiment; lines: simulation; (■, □) Run A1; (▲, △) Run B1; (●, ○) Run B2; (◆, ◇) Run B3; (⊠, ⊠) Run B4.

formance predicted by the model in terms of the light product purity (y_p) and butane vapor recovery (R) agreed well with the experimental results (Fig. 8). However, the predicted E's were again lower, deviating by −8.8% for Run B1 to −22.8% for Run B4, and the differences in the predicted and experimental BCF's ranged from 2.8 to 13.3%.

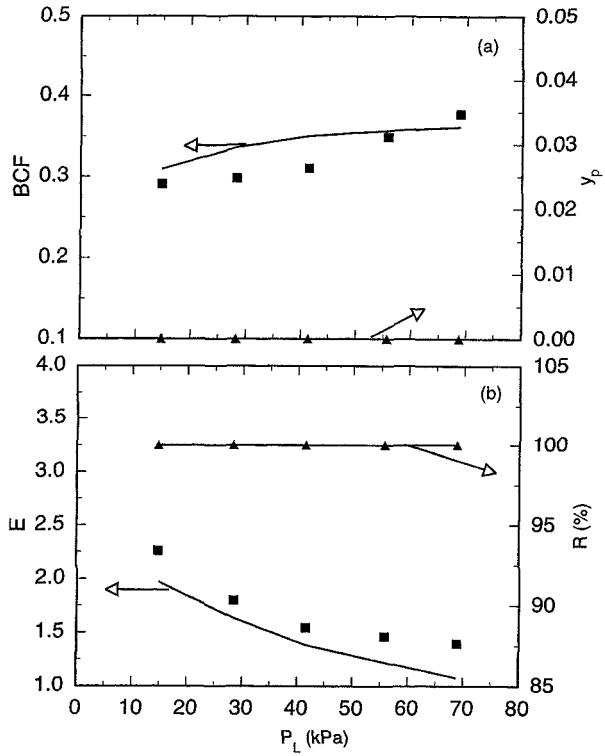

FIG. 8 Effect of the purge pressure (P_L) on the process performance in terms of the bed capacity factor (BCF), light product purity (y_p), butane vapor enrichment (E), and solvent vapor recovery (R). Symbols: experiment; line: simulation.

The simulated butane vapor concentration and temperature profiles at the beginning and end of the adsorption step of the series of runs (Runs C1 to C4) that were carried out to investigate the effect of the volumetric feed flow rate (V_f) are compared with the experimental profiles in Fig. 9. A comparison of the simulated and experimental process performances from these runs is given in Fig. 10. Note that P_L and γ inadvertently changed for the last two runs (C3 and C4) in this series of experiments. The changes in those two experimental parameters were also accounted for in the simulations; and accordingly, the model successfully predicted the changes in the bed profiles that were caused

by these subtle changes in P_L and γ (Fig. 9). The differences between the simulated and experimental results ranged from −4.0 to 0.0% for the BCF, 0.0 to 5.4% for R, −7.0 to −24.7% for E, and −31.3 to 0.0% for y_p.

The simulated butane vapor concentration and temperature profiles at the beginning and end of the adsorption step of the series of runs (Runs A1, and D1 to D3) that were carried out to investigate the effect of the feed mole fraction (y_f) are compared with the experimental profiles in Fig. 11. A com-

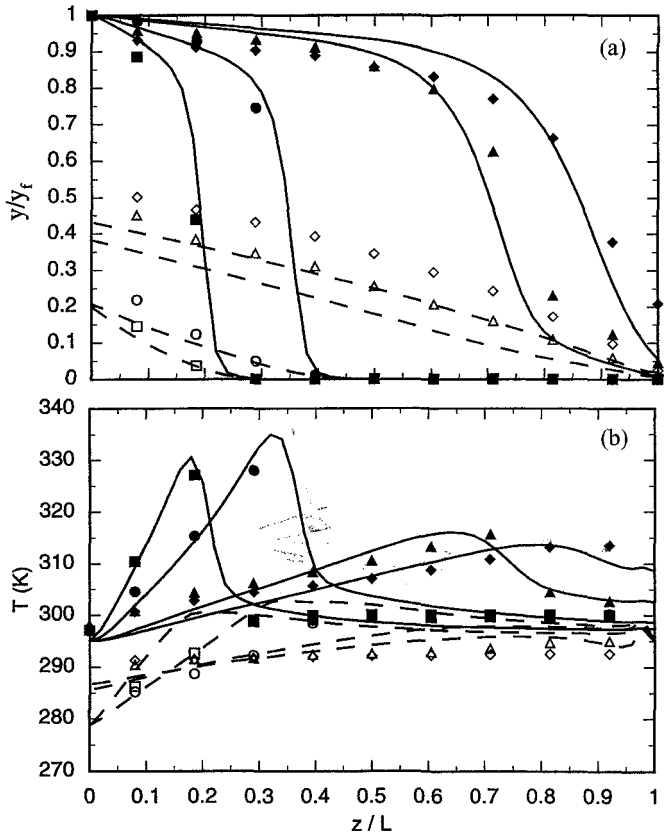

FIG. 9 Effect of the volumetric feed flow rate (V_f) on the (a) gas-phase mole fraction and (b) temperature profiles at the beginning (dashes) and end (solid lines) of the adsorption step. Symbols: experiment; lines: simulation; (■, □) Run C1; (▲, △) Run C2; (●, ○) Run C3; (◆, ◇) Run C4.

parison of the simulated and experimental process performances from these runs is given in Fig. 12. Figure 11 shows that for runs with a higher y_f (e.g., Run D3), the model predicted a sharper concentration profile (Fig. 11a) and higher temperature profile (Fig. 11b) than the experiment. However, the predicted E's became closer to those from the experiments when y_f became larger (Fig. 12b). For example, the predicted E was 15.7% lower for the run with a $y_f = 0.095$ (D1), and it was 5.8% lower for the run with a $y_f = 0.393$ (D3).

The simulated butane vapor concentration and temperature profiles at the beginning and end of the adsorption step of the series of runs (Runs E1 to E5) that were carried out to investigate the effect of the cycle time (t_c) are compared with the experimental profiles in Fig. 13. A comparison of the

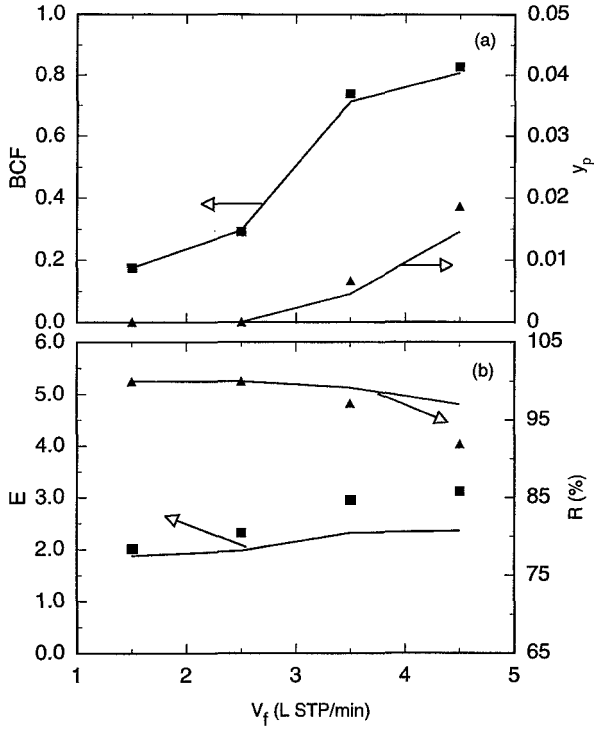

FIG. 10 Effect of the volumetric feed flow rate (V_f) on the process performance in terms of the bed capacity factor (BCF), light product purity (y_p), butane vapor enrichment (E), and solvent vapor recovery (R). Symbols: experiment; lines: simulation.

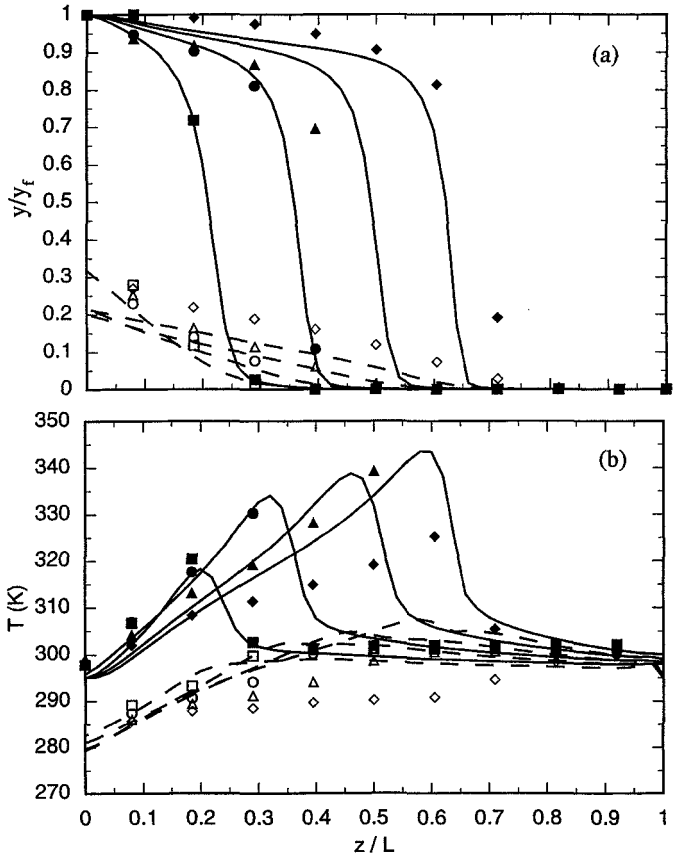

FIG. 11 Effect of the feed mole fraction (y_f) on the (a) gas-phase mole fraction and (b) temperature profiles at the beginning (dashes) and end (solid lines) of the adsorption step. Symbols: experiment; lines: simulation; (■, □) Run D1; (▲, △) Run A1; (●, ○) Run D2; (◆, ◇) Run D3.

simulated and experimental process performances from these runs is given in Fig. 14. Figure 13 shows that the model performs better for PSA cycles with a shorter cycle time (t_c) (e.g., Run E1), especially in terms of the temperature profiles (Fig. 13b). The percentage differences between the simulated and experimental process performances were 0.0 to −8.6% for the BCF, 0.0 to 4.3% for R, −0.7 to −18.8% for E, and −31.8 to −46.2% for y_p (Fig. 14 and Table 3). Note that the model predictions of y_p were consid-

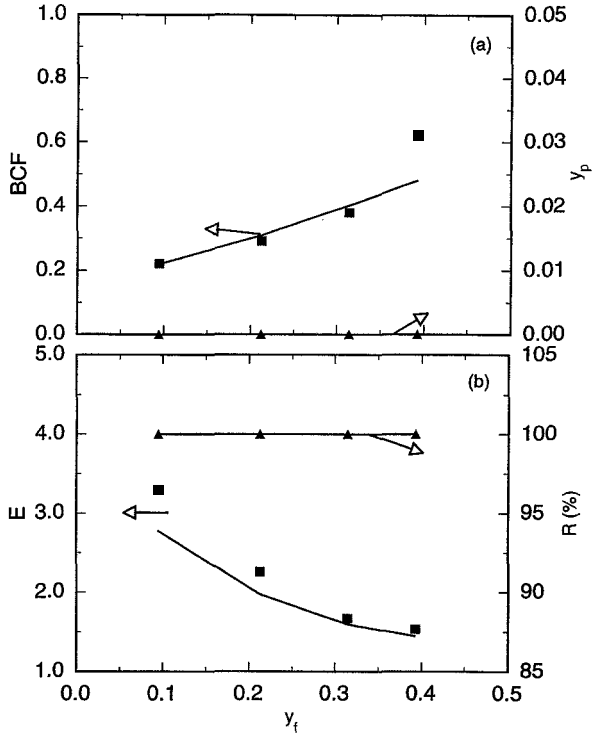

FIG. 12 Effect of the feed mole fraction (y_f) on the process performance in terms of the bed capacity factor (BCF), light product purity (y_p), butane vapor enrichment (E), and solvent vapor recovery (R). Symbols: experiment; lines: simulation.

ered to be very good; the apparent deviations were high because the absolute values of y_p were relatively small.

The simulated butane vapor concentration and temperature profiles at the beginning and end of the adsorption step of the series of runs (Runs E3, and F1 to F3) that were carried out to investigate the effect of the pressurization and blowdown step time (t_{pb}) are compared with the experimental profiles in Fig. 15. A comparison of the simulated and experimental process performances from these runs is given in Fig. 16. The model successfully predicted the insignificant effect of t_{pb} on the bed profiles and the process performance.

It even predicted the small jump in the concentration and temperature profiles from the first three runs (F1 to F3) to the last run (E3). Figure 15(b) shows that the largest deviations of the predicted temperature profiles from the experimental results occurred within the mass transfer zone, especially in the

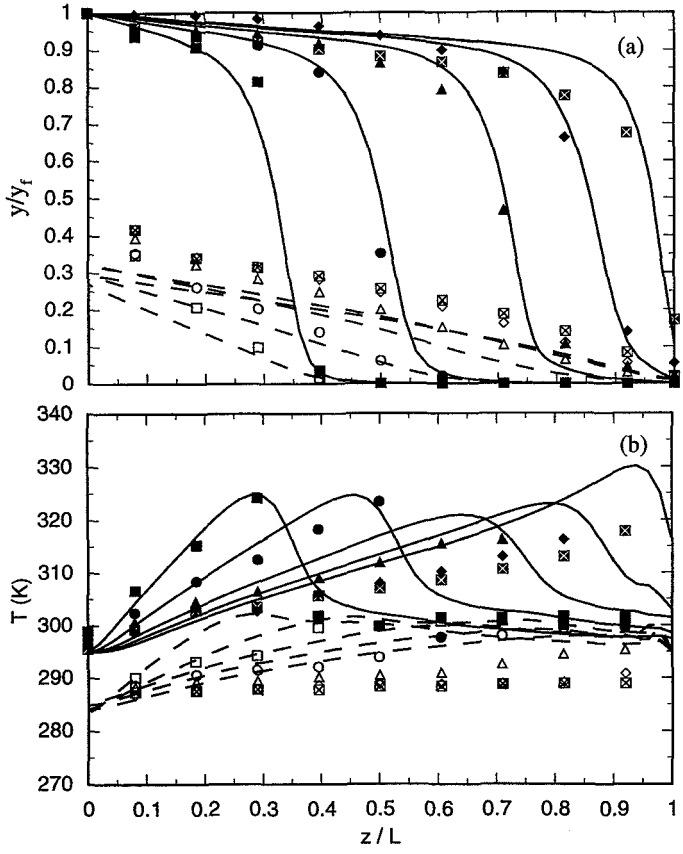

FIG. 13 Effect of the cycle time (t_c) on the (a) gas-phase mole fraction and (b) temperature profiles at the beginning (dashes) and end (solid lines) of the adsorption step. Symbols: experiment; lines: simulation; (■, □) Run E1; (▲, △) Run E2; (●, ○) Run E3; (◆, ◇) Run E4; (⊠, ⊠) Run E5.

regions close to the wave fronts. This deviation between experiment and simulation was also observed in the other five series of runs (see Figs. 5b, 7b, 9b, 11b, and 13b). As pointed out in the discussion of the process dynamics, the main source contributing to this deviation was perhaps the use of a constant overall heat transfer coefficient. The percentage deviations of the simulated process performance indicators from those obtained from experiments ranged from −16.5 to −19.9% for E, −0.2 to 0.2% for R, −4.5 to −12.5% for the BCF, and −37.9 to 7.1% for y_p.

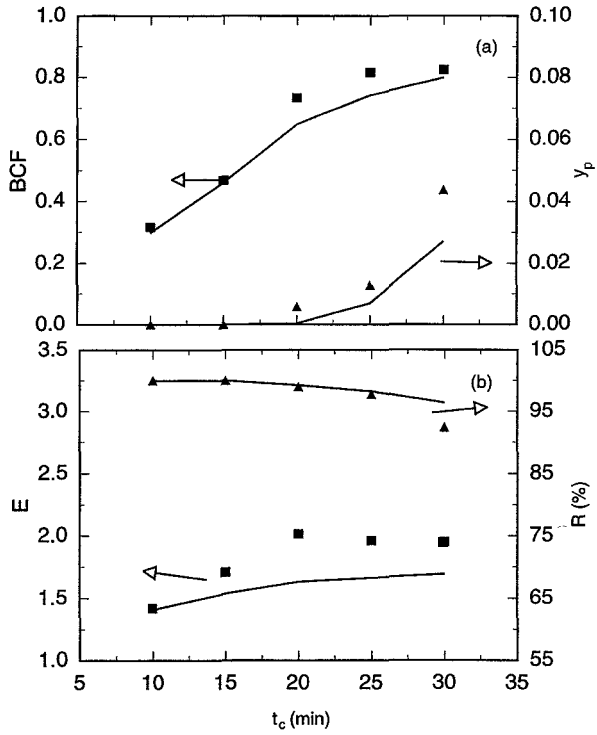

FIG. 14 Effect of the cycle time (t_c) on the process performance in terms of the bed capacity factor (BCF), light product purity (y_p), butane vapor enrichment (E), and solvent vapor recovery (R). Symbols: experiment; lines: simulation.

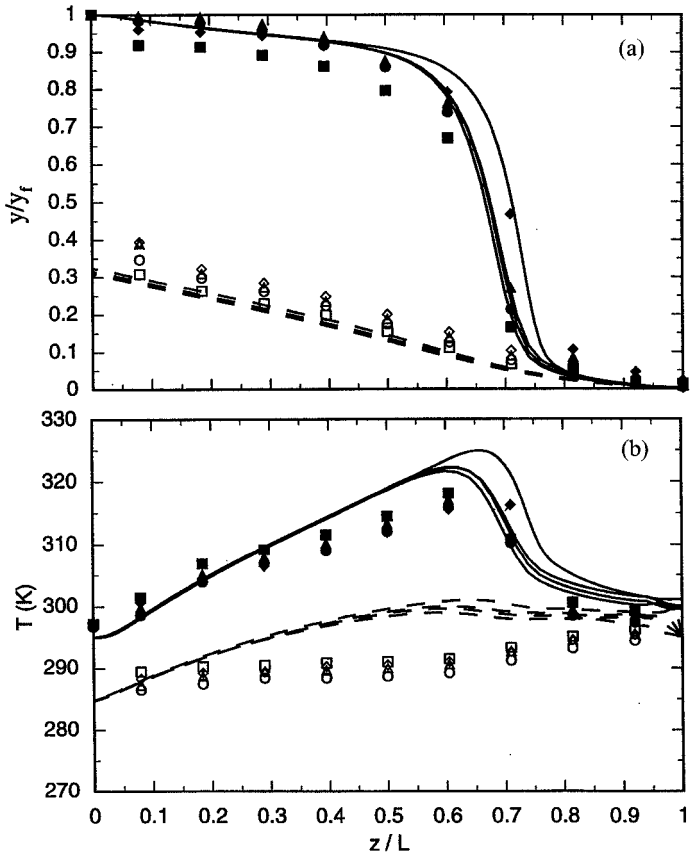

FIG. 15 Effect of the pressurization and blowdown step time (t_{pb}) on the (a) gas-phase mole fraction and (b) temperature profiles at the beginning (dashes) and end (solid lines) of the adsorption step. Symbols: experiment; lines: simulation; (■, □) Run F1; (▲, △) Run F2; (●, ○) Run F3; (◆, ◇) Run E3.

CONCLUSIONS

A fully predictive (no adjustable parameters), nonisothermal, multicomponent mathematical model was developed and used to simulate a PSA process that was designed for the separation and recovery of concentrated butane vapor from nitrogen using BAX activated carbon. This PSA model was unique in that it accounted for the temperature dependence of the gas-phase proper-

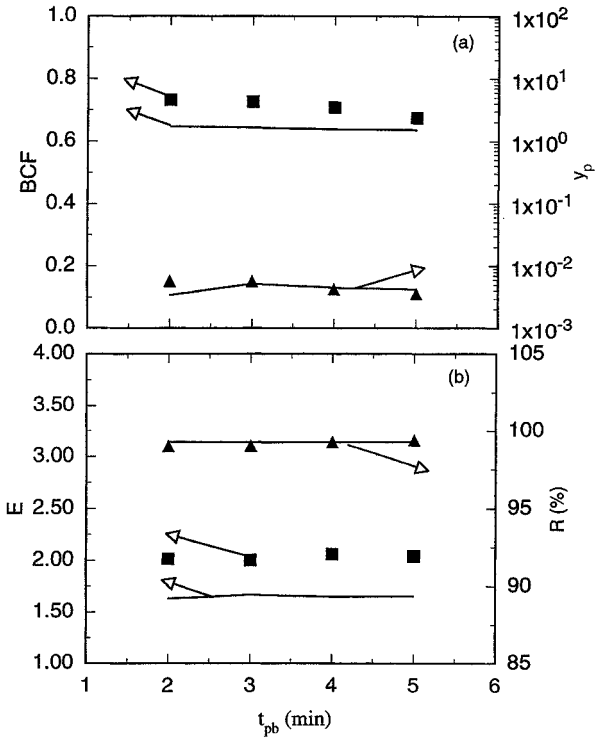

FIG. 16 Effect of the pressurization and blowdown step time (t_{pb}) on the process performance in terms of the bed capacity factor (BCF), light product purity (y_p), butane vapor enrichment (E), and solvent vapor recovery (R). Symbols: experiment; lines: simulation.

ties, the adsorbed-phase heat capacity, and a loading-dependent heat of adsorption. In simulating all of the cycle steps, the agreement with experiments was nearly quantitative in most cases, capturing both the transient and periodic behaviors. In fact, the model successfully predicted the high transient temperature swings which are critical to the successful design of such a PSA process. The trends observed from the simulation results were not only consistent with the experimental trends, they also verified some of the unique results obtained experimentally. For example, a unique periodic state was predicted when a PSA process was started either from clean or partially contaminated beds if the beds were more contaminated in the final periodic state than the initial condition. As predicted, the purge pressure did not have a significant effect on the bed profiles, but it did have a significant effect on the solvent vapor enrichment; and as predicted, the pressurization and blowdown step time had essen-

tially no effect on the process dynamics and performance.

The predicted periodic state process performances were also fairly good over a wide range of operating conditions; this was especially true for the predicted bed capacity factor, which was almost quantitative for most runs. The predicted butane vapor recoveries were 0 to 7.9% higher and the predicted butane vapor enrichments were 0.9–25.5% lower compared to the experimental results, depending on the process conditions. The percentage deviations of the predicted light product purity from the experimental results were relatively large (−50 to 0.0%); however, these percentage deviations are misleading because the butane vapor concentration in the light product was usually very small.

In general, the model performed very well considering that no adjustable parameters were used, and that the LDF approximation and an overall heat transfer coefficient were both utilized to minimize the computational time. Some consistent deviations between the simulated and experimental results, such as the higher predicted temperature profiles at the beginning of the adsorption step (i.e., at the end of the purge step) and the lower solvent vapor enrichment, indicated that a better pressure history during the desorption step, a cycle-time-dependent mass transfer coefficient in the LDF approximation, and a fluid-phase velocity-dependent overall heat transfer coefficient may improve the accuracy of these simulated results.

NOMENCLATURE

A	coefficient for the gas-phase heat capacity (kJ/mol·K)
B	coefficient for the gas-phase heat capacity (kJ/mol·K^2)
BCF	bed capacity factor
b, b^0	adsorption isotherm parameters (kPa^{-1})
C	coefficient for the gas-phase heat capacity (kJ/mol·K^3)
Cp_a	adsorbed-phase capacity (kJ/mol·K)
Cp_g	gas-phase heat capacity (kJ/mol·K)
Cp_s	solid-phase (pellet) heat capacity (kJ/kg·K)
D	coefficient for the gas-phase heat capacity (kJ/mol·K^4)
E	solvent vapor enrichment
h	overall heat transfer coefficient (kJ/m^2·s·K)
ΔH	isosteric heat of adsorption (kJ/mol)
k	mass transfer coefficient (s^{-1})
L	bed length (m)
P	pressure (kPa)
P_H	high pressure feed (kPa)
P_L	low pressure purge (kPa)
q_i	adsorbate loading (mol/kg)
q_m, q_0	adsorption isotherm parameters (mol/kg)

q_i^*	equilibrium amount adsorbed (mol/kg)
R	gas constant, or solvent vapor recovery
S_i	defined by Eq. (3)
t	time (s)
t_c	cycle time (s)
T	temperature (K)
T_0	ambient temperature (K)
u	interstitial velocity (m/s)
V_f	feed volumetric flow rate (m^3/min)
y	gas-phase mole fraction
y_p	time-averaged solvent vapor mole fraction in the light product
z	axial position in the column (m)

Greek Letters

ρ_s	adsorbent pellet density (kg/m^3)
ε	interstitial void fraction in the column
γ	volumetric purge-to-feed ratio

Subscripts

cal	calculated
exp	experimental
f	feed
H	high
i	component index
L	low
pb	pressurization and blowdown
p	light product or purge
I, II, III, IV	step numbers

ACKNOWLEDGMENTS

The authors gratefully acknowledge financial support from the National Science Foundation under Grant CTS-9410630, and from the Westvaco Charleston Research Center.

REFERENCES

1. Y. Liu, C. E. Holland, and J. A. Ritter, "Solvent Vapor Recovery by Pressure Swing Adsorption. I. Experimental Transient and Periodic Dynamics of the Butane–Activated Carbon System," *Sep. Sci. Technol.*, *33*, 2311–2334 (1998).
2. Y. Liu, C. E. Holland, and J. A. Ritter, "Solvent Vapor Recovery by Pressure Swing Ad-

sorption. II. Experimental Periodic Performance of the Butane–Activated Carbon System," *Ibid.*, *33*, 2431–2464 (1998).
3. R. T. Yang, *Gas Separation by Adsorption Process*, Butterworth, London, 1986.
4. D. M. Ruthven, S. Farooq and K. S. Knaebel, *Pressure Swing Adsorption*, VCH Publishers, New York, NY, 1994.
5. L. H. Shendalman and J. E. Mitchell, "A Study of Heatless Adsorption in the Model System CO_2 in He, I," *Chem. Eng. Sci.*, *27*, 1449–1458 (1972).
6. Y. N. I. Chan, F. B. Hill, and Y. W. Wong, "Equilibrium Theory of a Pressure Swing Adsorption Process," *Ibid.*, *36*, 243–251 (1981).
7. F. G. Flores and C. N. Kenney, "Modeling of the Pressure Swing Air Separation Process," *Ibid.*, *38*, 827–834 (1983).
8. K. S. Knaebel and F. B. Hill, "Pressure Swing Adsorption: Development of an Equilibrium Theory for Gas Separations," *Ibid.*, *40*, 2351–2360 (1985).
9. M. D. LeVan, "Pressure Swing Adsorption: Equilibrium Theory for Purification and Enrichment," *Ind. Eng. Chem. Res.*, *34*, 2655–2600 (1995).
10. D. Subramanian and J. A. Ritter, "Equilibrium Theory for Solvent Vapor Recovery by Pressure Swing Adsorption: Analytical Solution for Process Performance," *Chem. Eng. Sci.*, *52*, 3147–3160 (1997).
11. D. Subramanian, J. A. Ritter, and Y. Liu, "Equilibrium Theory for Solvent Vapor Recovery by Pressure Swing Adsorption: Analytic Solution for Process Performance with Velocity Variation and Gas Phase Capacitance," *Chem. Eng. Sci.*, *54*, 475–481 (1999).
12. Y. Liu and J. A. Ritter, "Fractional Factorial Study of a Pressure Swing Adsorption-Solvent Vapor Recovery Process," *Adsorption*, *3*, 151–163 (1997).
13. Y. Liu and J. A. Ritter, "Evaluation of Model Approximations in Simulating Pressure Swing Adsorption-Solvent Vapor Recovery," *Ind. Eng. Chem. Res.*, *36*, 1767–1778 (1997).
14. N. S. Raghavan, M. M. Hassan, and D. M. Ruthven, *Chem. Eng. Sci.*, *41*, 2787 (1986).
15. H. S. Shin and K. S. Knaebel, *AIChE J.*, *33*, 654 (1987).
16. R. T. Yang and S. J. Doong, "Gas Separation by Pressure Swing Adsorption: A Pore-Diffusion Model for Bulk Separation," *Ibid.*, *31*, 1829–1842 (1985).
17. S. J. Doong and R. T. Yang, "Bulk Separation of Multicomponent Gas Mixture by Pressure Swing Adsorption: Pore/Surface Diffusion and Equilibrium Models," *Ibid.*, *32*, 397–410 (1986).
18. S. J. Doong and R. T. Yang, "Bidisperse Pore Diffusion Model for Zeolite Pressure Swing Adsorption," *Ibid.*, *33*, 1045–1049 (1987).
19. S. Nakao and M. Suzuki, "Mass Transfer Coefficient in Cyclic Adsorption and Desorption," *J. Chem. Eng. Jpn.*, *16*, 114–119 (1983).
20. J. A. Ritter and R. T. Yang, "Pressure Swing Adsorption: Experimental and Theoretical Study on Air Purification and Vapor Recovery," *Ind. Eng. Chem. Res.*, *30*, 1023–1032 (1991).
21. E. S., Kikkinides, J. A. Ritter, and R. T. Yang, "Pressure Swing Adsorption for Simultaneous Purification and Sorbate Recovery," *J. Chin. Inst. Chem. Eng.*, *22*, 399 (1991).
22. Y. Liu and J. A. Ritter, "Pressure Swing Adsorption-Solvent Vapor Recovery: Process Dynamics and Parametric Study," *Ind. Eng. Chem. Res.*, *35*, 2299–2312 (1996).
23. Y. Liu and J. A. Ritter, "Periodic State Heat Effects in Pressure Swing Adsorption-Solvent Vapor Recovery," *Adsorption*, *4*, 159–172 (1998).
24. S. Farooq and D. M. Ruthven, "Heat Effects in Adsorption Column Dynamics. 2. Experimental Validation of the One-Dimensional Model," *Ind. Eng. Chem. Res.*, *29*, 1084–1090 (1990).
25. R. S. Drago, D. S. Burns, and T. J. Lafrenz, "A New Adsorption Model for Analyzing Gas-Solid Equilibria in Porous Materials," *J. Phys. Chem.*, *100*, 1718–1724 (1996).

26. Y. Liu, J. Delgado, and J. A. Ritter, "Comparison of Finite Difference Techniques for Simulating Pressure Swing Adsorption," *Adsorption*, *4*, 337–344 (1998).
27. Y. Liu, S. P. Shealy, and J. A. Ritter, "Prediction of the Adsorbed Phase Heat Capacity," in *Preprints of Topical Conference on Separation Science and Technologies, Part II*, AIChE, New York, NY, 1997, pp. 990–995.
28. D. P. Valenzuela and A. L. Myers, *Adsorption Equilibria Data Handbook*, Prentice-Hall, Englewood Cliffs, NJ, 1989.
29. D. M. Ruthven, "Diffusion of Oxygen and Nitrogen in Carbon Molecular Sieves," *Chem. Eng. Sci.*, *47*, 4305–4308 (1992).
30. S. Kaguei, Q. Yu, and N. Wakao, "Thermal Waves in Adsorption Column. Parameter Estimation," *Ibid.*, *40*, 1069–1076 (1985).

Received by editor March 26, 1998
Revision received September 1998